

Systematic design of highly birefringent photonic crystal fibers

Jui-Ming Hsu¹

Received: 9 March 2016 / Accepted: 1 February 2017 / Published online: 27 February 2017
© Springer-Verlag Berlin Heidelberg 2017

Abstract This article systematically designs and theoretically investigates a highly birefringent photonic crystal fiber (HB-PCF) for reducing the effect of polarization mode dispersion in high-speed optical communication system. To achieve a high modal birefringence in the proposed HB-PCF, four types of HB-PCF were designed by adding some birefringence-enhancing factors step by step in sequence. Ultimately, as per the simulation results, in the condition of single-mode operation, the numeric values of modal birefringence and confinement loss of the proposed HB-PCF is about 21.85×10^{-3} and 0.47 dB/km at the habitual wavelength $\lambda = 1.55 \mu\text{m}$ of optical-fiber communications.

1 Introduction

Some imperfections of a single-mode fiber (SMF) are produced due to variations in geometric shape or impurity introducing in practical fiber-fabrication processes, and anisotropic stress acting on the fiber due to the fiber spanning in an optical communication system. These imperfections result in an uncontrolled and unpredictable modal birefringence in the SMF and bring about polarization mode dispersion (PMD). The PMD induces pulse broadening and seriously restricts the data rate in a high-speed optical communication link. The highly birefringent fibers (HBFs) were used to reduce the governing factor of small random birefringence fluctuations significantly. Conventional HBFs (such as elliptical core fibers, bowtie structured fibers, and

PANDA fibers) have a modal birefringence with a value of about 10^{-4} order typically. Recently many articles used photonic crystal fibers (PCFs) to realize highly birefringent photonic crystal fibers (HB-PCFs) [1–14]. Modal birefringence of about 10^{-3} order was achieved typically for most of these HB-PCFs at a wavelength of $1.55 \mu\text{m}$. In addition to the application of optical communication systems, HBFs also have been widely used for polarization control in optical modulators, Raman amplifiers [15], polarization splitters [16], fiber-optic sensors [5, 17], fiber gyroscopes [18], etc.

To introduce and enlarge the modal birefringence in PCFs, one can destroy the sixfold symmetry of the fiber to the best of one's ability and strongly split the degeneration doublet pair. Several approaches were proposed to destroy the symmetry of a PCF structure, such as setting some defective holes near the core [1–6] or a row of cladding [7]. Yang et al. used the complex unit cells in cladding [8]. Various structures of HB-PCFs employed a cladding with two differently sized squeezed elliptical air holes [9–11]. In addition, hybrid cladding structure [12], and rectangular centric rings of smaller circular air holes in the fiber core [13] were adopted to achieve high birefringence in a PCF. Chau [14] proposed a HB-PCF with rectangular air holes in cladding, which earned an ultrahigh birefringence of 81×10^{-3} at $\lambda = 1.55 \mu\text{m}$. However, the fabrication is quite hard to realize rectangular air holes. The modal birefringence B of a fiber is defined as the difference in effective index, which is denoted as n_{eff} in the paper, of the splitting modes

$$B = \left| n_{\text{eff}}^x - n_{\text{eff}}^y \right|, \quad (1)$$

where n_{eff}^x and n_{eff}^y are the effective indices of the x - and y -polarization mode, respectively.

✉ Jui-Ming Hsu
juiminghsu@gmail.com

¹ Department of Electro-Optical Engineering, National United University, Miaoli 360, Taiwan, Republic of China

In this paper, to achieve a high modal birefringence in a PCF, some birefringence-enhancing factors (BEFs) were superimposed step by step, and enlarged the difference between the effective indices of the degenerated fundamental modes. According to Eq. (1), a HB-PCF with ultrahigh birefringence was then achieved. In addition to the modal birefringence, the modal property and confinement loss of the proposed HB-PCF will be discussed for single-mode operation and low loss. The numeric results reveal that the proposed HB-PCF is operated in single mode, the value of modal birefringence is up to 21.85×10^{-3} , and the confinement loss is about 0.47 dB/km, at a wavelength of $1.55 \mu\text{m}$.

2 Simulation models and principles

In this work, the effective refractive indices of some modes, such as the splitting degeneration fundamental modes (n_{eff}^x and n_{eff}^y), the fundamental space-filling mode in the cladding area (n_{FSM}), and the second-order mode ($n_{2\text{eff}}$), were estimated using the plane-wave expansion (PWE) method. The PWE method is based on the plane-wave expansion of the electromagnetic field using Bloch's theorem. It is ideal for producing band structures for PCFs; moreover, it can be used to measure the modal properties such as effective index and mode area. In PWE simulation, the supercell approximation is used to treat a defect (core) region. It is worth noting that the supercell has to be large enough to determine the properties of the core region accurately [19].

2.1 Modal properties

To avoid the modal dispersion, birefringent fibers have to keep the propagation light in a single mode at the working wavelength. As an example, the modal property of a regular index-guiding PCF shown in Fig. 1a is investigated first. In the figure, the cladding of the PCF consists of seven layers of triangular lattices of air holes, referred to as cladding holes in this paper, each one with a diameter of d_c and a pitch Λ (center-to-center distance between the holes) of $3.00 \mu\text{m}$ in a background of undoped silica, whose refractive index can be estimated using the Sellmeier equation [20]:

$$n(\lambda) = \left[1 + \frac{0.6961663\lambda^2}{\lambda^2 - (0.0684043)^2} + \frac{0.4079426\lambda^2}{\lambda^2 - (0.1162414)^2} + \frac{0.8974794\lambda^2}{\lambda^2 - (9.896161)^2} \right]^{1/2}, \quad (2)$$

where λ is the operating wavelength. The solid core is formed by removing the central air hole. Figure 1b reveals the relationship between the normalized cutoff frequency (Λ/λ_c) of the second-order mode and the space-filling ratio of the cladding (d_c/Λ) for a regular PCF in Fig. 1a. To calculate the cutoff wavelength λ_c , one can first estimate the

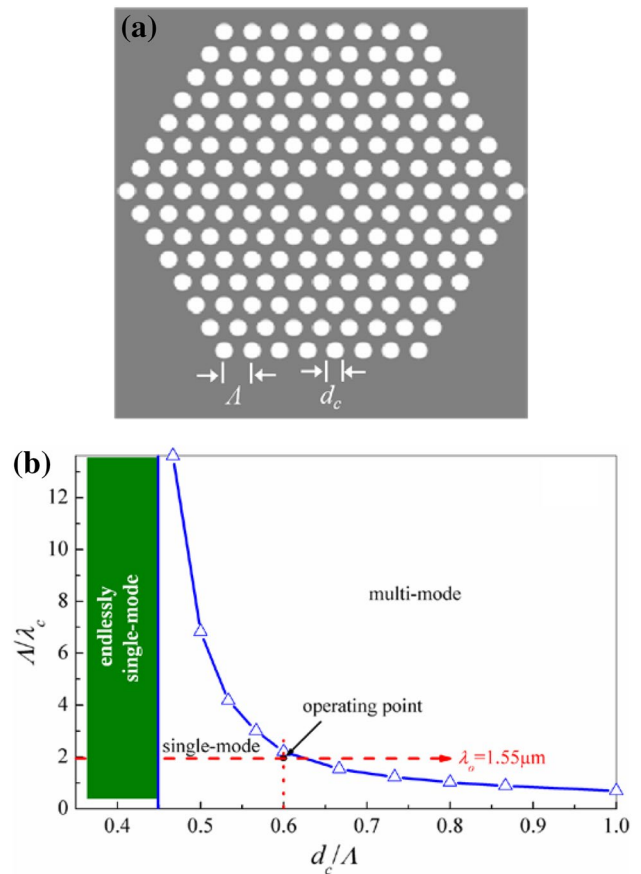


Fig. 1 **a** Cross-sectional view of a regular PCF. **b** Relationship between the normalized cutoff frequency (Λ/λ_c) of the second-order mode and the space-filling factor (d_c/Λ) of the cladding. The parameters at the operating point are $\Lambda = 3.00 \mu\text{m}$, $d_c = 1.80 \mu\text{m}$

mode index of the second-order mode $n_{2\text{eff}}$, and then find out a wavelength λ_c to satisfy the condition $n_{2\text{eff}} \leq n_{\text{FSM}}$, where FSM represents the fundamental space-filling mode in the cladding area [21]. The curve with triangle symbols defines a boundary of single- and multi-mode regime, above the curve the PCF is multi-mode, and below it is single mode. Furthermore, there is an endless single-mode regime for $d_c/\Lambda < 0.45$ [22]. The operating point represents the mode of the regular PCF at an operating wavelength of $\lambda_0 = 1.55 \mu\text{m}$ ($d_c/\Lambda = 0.6$, $\Lambda/\lambda_0 = 3/1.55$), it is located in the single-mode region as evident from the figure. In other words, to keep the propagation light in a single mode at a wavelength of $1.55 \mu\text{m}$, the cladding holes with a diameter of $d_c = 0.6 \times \Lambda = 1.80 \mu\text{m}$ is an appropriate design. For all investigated types, the variation of Λ/λ_c with the different core structure is slight, which will be shown in the subsequent Sect. 3.3 (Fig. 7). Therefore, the $d_c = 1.80 \mu\text{m}$ is determined for this work. The modal properties of the proposed structures will be examined in Sect. 3.3.

2.2 Simulation models and modal birefringence

For comparison, Fig. 2a shows the cross-sectional view of a regular PCF with $d_c = 1.80 \mu\text{m}$ and $\Lambda = 3.00 \mu\text{m}$, which is the same as Fig. 1a.

To destroy the sixfold symmetry of the fiber, split the degeneration doublet pair, and enlarge the modal birefringence, the first BEF (BEF-1)—replacing four air holes at the innermost cladding layer of the PCF with larger holes with a diameter of $d_l = 2.80 \mu\text{m}$ —is introduced. This type of structure is named as Type 1 in this article, and the cross-sectional view of HB-PCF Type 1 is indicated in Fig. 2b. To show the effect of each BEF-adding, the effective indices of splitting degeneration modes for the different types of HB-PCFs are compared and indicated in Fig. 3. In Fig. 3a, for the regular PCF, the n_{eff}^x and n_{eff}^y are identical at all of wavelength due to the sixfold symmetry of the PCF. According to Eq. (1), the modal birefringence values, which can be simplified as B values, of an ideal regular PCF are zero for the entire band. For the HB-PCF Type 1, the effective indices of the two degeneration modes are split due to the destruction of sixfold symmetry by introducing the BEF-1, and the B values arise at some wavelengths.

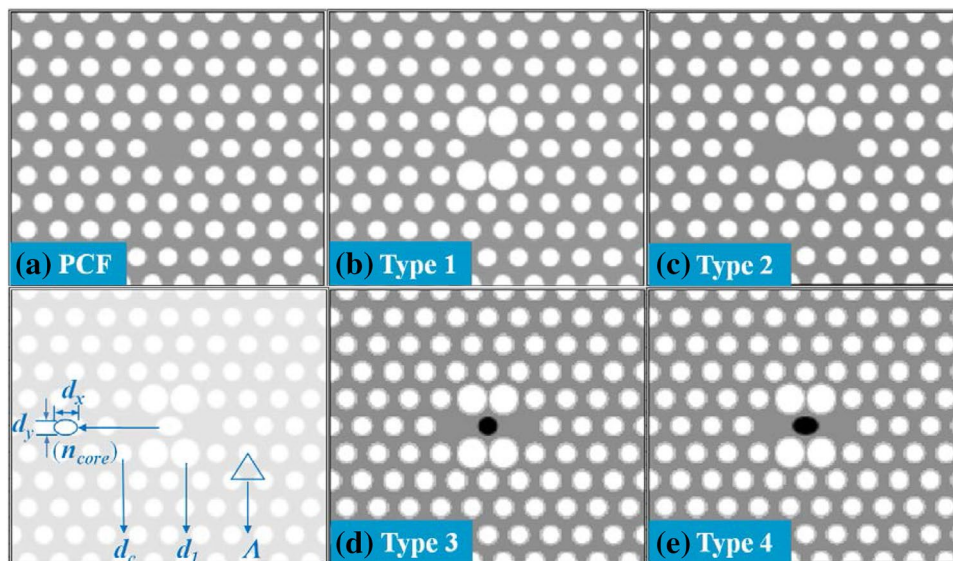
To enhance the asymmetry of the PCF structure, split the degeneration doublet pair, and enlarge the modal birefringence even more, in addition to the BEF-1, the second BEF (BEF-2)—a removal of two holes in the appropriate orientation at the innermost layer of the PCF—is added. This type of HB-PCF is named as Type 2, and the cross-sectional view of HB-PCF Type 2 is shown in Fig. 2c. The comparison between n_{eff}^x and n_{eff}^y for HB-PCF Type 1 and 2 is demonstrated in Fig. 3b. It is obvious in the figure that the separation of effective index curves (n_{eff} -curves) between the splitting degeneration doublet pair (x - and

y -mode) for the HB-PCF Type 2 is wider than that for the HB-PCF Type 1 at some wavelengths. Thus, one can predict, according to Fig. 3b, that the B values of the HB-PCF Type 2 are larger than that of Type 1 at some wavelengths, and this enlarging factor results from the introduction of BEF-2.

To increase the birefringence more, one can strengthen the confinement of the splitting degeneration modes in the core region. Therefore, the third BEF (BEF-3) is added by increasing the refractive index of the core. The HB-PCF Type 3 shown in Fig. 2d was designed by inserting a circular Ge-doped rod with a diameter of $1.80 \mu\text{m}$, which is the same with the cladding holes, and a high refractive index of $n_{\text{core}} = 1.560$ at a wavelength of $1.55 \mu\text{m}$ in the center of the core. Figure 3c compares the n_{eff}^x with n_{eff}^y for HB-PCF Type 2 and 3. Because of introducing the BEF-3, the separation of n_{eff} -curves between the two splitting degeneration modes for the HB-PCF Type 3 is wider than that for the HB-PCF Type 2, and larger B values of the HB-PCF Type 3 compared to those of the Type 2 can be predictable at some wavelengths.

Ultimately, introducing the fourth BEF (BEF-4) into the HB-PCF Type 3 to even more enlarge the modal birefringence and accomplish the final structure—HB-PCF Type 4. For the BEF-4, the circular Ge-doped rod in the HB-PCF Type 3 is replaced with an elliptical one with the same refractive index, which increases the n_{eff} component at x -orientation, as shown in Fig. 2e. In this work, the lengths of major and minor axis of the central elliptic rod are $d_y = d_c = 1.80 \mu\text{m}$ and $d_x = 2.52 \mu\text{m}$, respectively. Figure 3d shows the comparison between the n_{eff}^x and n_{eff}^y for the HB-PCF Type 3 and 4. As shown in the figure, the separation of n_{eff} -curves between the two splitting degeneration modes for the HB-PCF Type 4 is wider than that for

Fig. 2 Cross-sectional views of **a** a regular PCF and the HB-PCFs, **b** Type 1, **c** Type 2, **d** Type 3, and **e** Type 4. $\Lambda = 3.00 \mu\text{m}$, $d_c = d_y = 1.80 \mu\text{m}$, $d_l = 2.80 \mu\text{m}$, $d_x = 2.52 \mu\text{m}$, $n_{\text{core}} = 1.560$ at a wavelength of $1.55 \mu\text{m}$



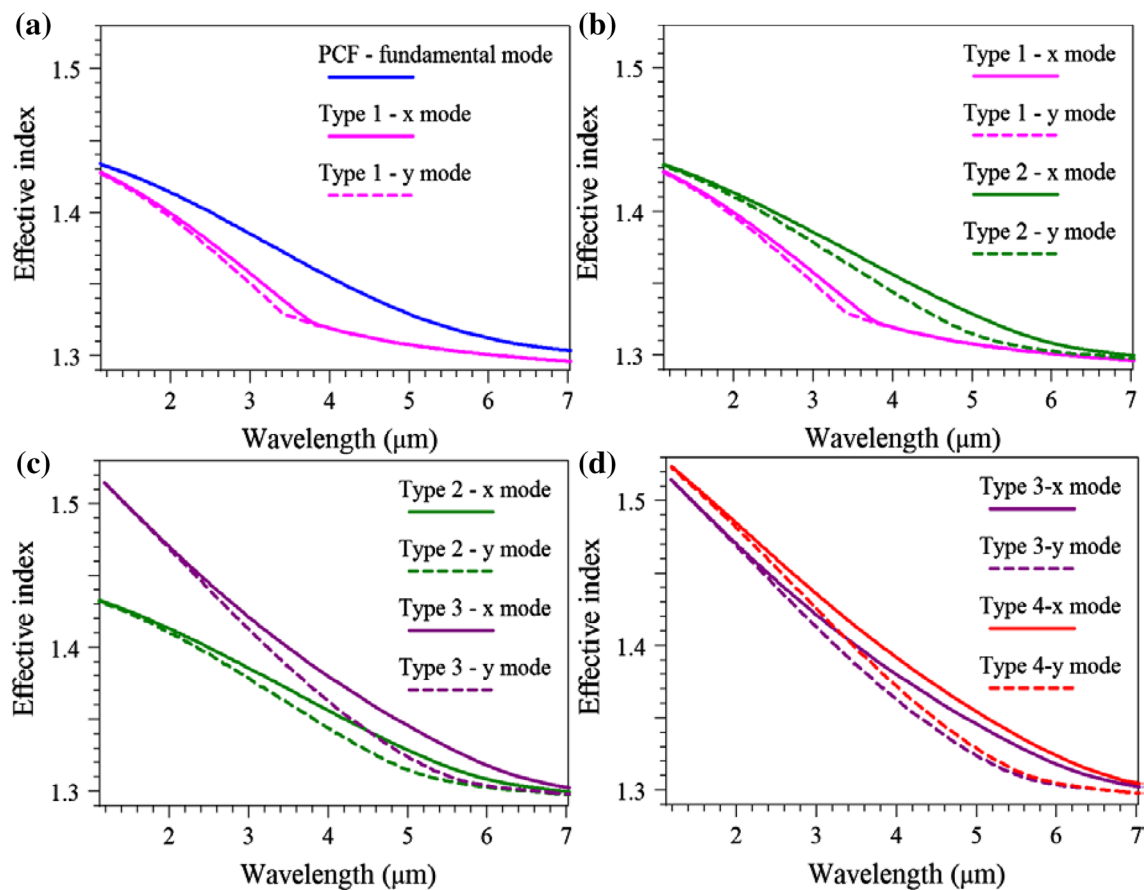


Fig. 3 Comparing the effective indices (n_{eff}) of splitting degeneration modes between the **a** regular PCF and Type 1, **b** Type 1 and Type 2, **c** Type 2 and Type 3, and **d** Type 3 and Type 4 HB-PCFs as shown in Fig. 2

the HB-PCF Type 3 due to the introducing of BEF-4. One can anticipate that the modal birefringence of the HB-PCF Type 4 is largest in the four types of HB-PCFs.

2.3 Confinement loss

The loss is another important parameter for a HB-PCF used in a communication link. The confinement losses (L_C) for each case can be deduced by the imaginary part of effective indices (n_{eff}) as

$$L_C = 8.686 \times k_0 \times \text{Im}[n_{\text{eff}}], \quad (3)$$

where k_0 is the wave number in free space, $\text{Im}[n_{\text{eff}}]$ represents the imaginary part of n_{eff} . The $\text{Im}[n_{\text{eff}}]$'s of the four types of the HB-PCFs can be calculated using the beam propagation method (BPM), and then substitute the $\text{Im}[n_{\text{eff}}]$'s into Eq. (3) to estimate the confinement losses. The BPM is currently the most widely used for the study of light propagation in longitudinally varying optical waveguides; its drawback is difficult to take into account backward reflecting waves [19].

3 Numerical results and discussions

3.1 Modal birefringence (B)

The refractive indices of the splitting degeneration modes n_{eff}^x and n_{eff}^y were estimated by means of the above-mentioned PWE method, and then the modal birefringence B 's were deduced using Eq. (1). Figure 4 compares the B values of these four types of HB-PCF. As shown in the figure, the maximum B values increase in sequence of adding the BEF-1 to BEF-4, respectively, as expected in the preceding discussion.

The birefringence curve (B -curve) of Type 1 decreases sharply between a wavelength range of 3.4–3.8 μm , this can be clearly deduced from Fig. 3a. As per the n_{eff} -curves of Type 1 in Fig. 3a, the curves of y and x modes have breaking points at a wavelength of 3.4 and 3.8 μm , respectively. The n_{eff} -curve of Type 1- y -mode is raised for the wavelengths longer than 3.4 μm . Thus, according to Eq. (1), the B -curve of Type 1 has a sharp decline between 3.4 and 3.8 μm . The occurrence of breaking points for the n_{eff} -curves of Type 1 can be explained

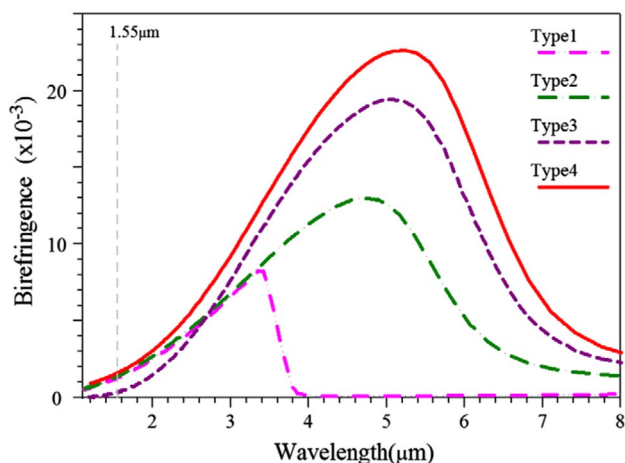


Fig. 4 Dependence of birefringence on wavelength for the HB-PCF Type 1 to 4. $\Lambda = 3.00 \mu\text{m}$, $d_c = d_y = 1.80 \mu\text{m}$, $d_1 = 2.80 \mu\text{m}$, $d_x = 2.52 \mu\text{m}$, $n_{\text{core}} = 1.560$ at a wavelength of $1.55 \mu\text{m}$

as follows. For a shorter- λ region, as the wavelength increases, the x and y modes gradually extend their fields into the innermost layer, which includes four large holes in y -direction as shown in Fig. 2b. Therefore, the n_{eff} decreases drastically with wavelength. For a longer- λ region, the modes stretch out their fields further into the outer cladding with smaller holes. Accordingly, the n_{eff} decreases gently with wavelength, and then the breaking points are formed between the two regions. By contrast, the breaking effect on the other types of HB-PCF is unobvious, this results in a fact that the B-curve of Type 1 as shown in Fig. 4 shows quite different behavior from other types. The reason of unobvious breaking effect for other types of HB-PCF is explained as follows. For Type 2–4, as shown in Fig. 2, two smaller holes at the innermost layer are removed. Therefore, some field will be distributed in the imperforate region. In addition, Type 3 and 4 confine the mode fields severely in the core regions due to the higher n_{core} . These two causes reduce the power extended into the outer cladding region with smaller holes, and bring about a result that the extended power is not enough to achieve an obvious breaking effect.

3.2 Blue-tune by shrinking

As per Fig. 4, for all types of the HB-PCFs, the maximum B value occurred at a wavelength λ_{max} far from the habitual wavelength of $1.55 \mu\text{m}$ in optical-fiber communication. To shift λ_{max} toward a shorter wavelength (blue-tune) while still keeping its birefringence at an original maximum B value, one can shrink the whole structure with a shrink

ratio of α ($\alpha < 1$) [3]. On the other hand, one can expand the whole structure with an expand ratio of β ($\beta > 1$) to shift λ_{max} toward a longer wavelength (red-tune). The blue-tuning/red-tuning method scales down/up all the geometric parameters (Λ , d_1 , d_c , d_x and d_y) simultaneously with a same ratio of α/β . In this work, to shift λ_{max} toward a wavelength of $1.55 \mu\text{m}$, the B curves of all types of the HB-PCF need to be blue-tuned by a different ratio of α . Figure 5 shows the relationship between the B curves and wavelength for the four types of the HB-PCF with various α . As shown in the figures, the B curves are blue-tuned with a smaller α , and the maximum B values are nearly identical with various α for each type of the HB-PCF.

Figure 6 indicates the dependence of the λ_{max} on the shrink ratio α for the four types of the HB-PCF. For $\alpha = 1$, which is the case shown in Fig. 4, the λ_{max} s are located at the wavelengths of 3.36 , 4.77 , 5.07 , and $5.24 \mu\text{m}$ with respect to Type 1 to Type 4. Furthermore, as per the figure, to shift λ_{max} s to $1.55 \mu\text{m}$, the required values of α s are 0.4586 , 0.3269 , 0.3066 and 0.2992 (which are directed by the arrows in the figure) for Type 1 to Type 4, respectively. To achieve a maximum B value at the wavelength of $1.55 \mu\text{m}$, one can blue-tune the λ_{max} to the wavelength of $1.55 \mu\text{m}$ by shrinking the original HB-PCF structure with the ratio of α as given above. However, it is not a good design because the single-mode operation and the confinement loss are not taken into account.

3.3 Modal properties

According to Fig. 4, the HB-PCF Type 1 and 2 can be disregarded in the work due to their small birefringence. To examine the modal properties for the HB-PCF Type 3 and 4 with $d_c/\Lambda = 0.6$, the relationship between the normalized cutoff frequencies ($\Lambda/\lambda_{\text{cx}}$, x is 3 or 4 for HB-PCF Type 3 and 4, respectively) of the second order mode for Type 3 and 4, the normalized operating frequency (Λ/λ_o , where $\lambda_o = 1.55 \mu\text{m}$) and the shrink ratios (α) are estimated and demonstrated in Fig. 7. As shown in the figure, the variations of the normalized cutoff frequencies of the second-order mode $\Lambda/\lambda_{\text{cx}}$ for the Type 3 and 4 are slight. As mentioned in Sect. 2.1, the condition of single-mode operation is $\Lambda/\lambda_o < \Lambda/\lambda_{\text{cx}}$. Thus, the critical shrink ratios α_{cx} were defined by the conditions of $\Lambda/\lambda_o = \Lambda/\lambda_{\text{cx}}$, they are the boundaries between the single- and multi-mode regions for the α value. As per the figure, the HB-PCFs operate in single mode for the cases of $\alpha < \alpha_{\text{cx}}$, while in multi-modes for $\alpha > \alpha_{\text{cx}}$. The numerical results revealed that $\alpha_{\text{c3}} = 0.3370$ and $\alpha_{\text{c4}} = 0.3316$.

Figure 8a–d indicates the field patterns of intensity components $|E_x|^2$ and $|E_y|^2$ for the x - and y -polarized fundamental modes for the HB-PCF Type 1 to 4 at a wavelength of

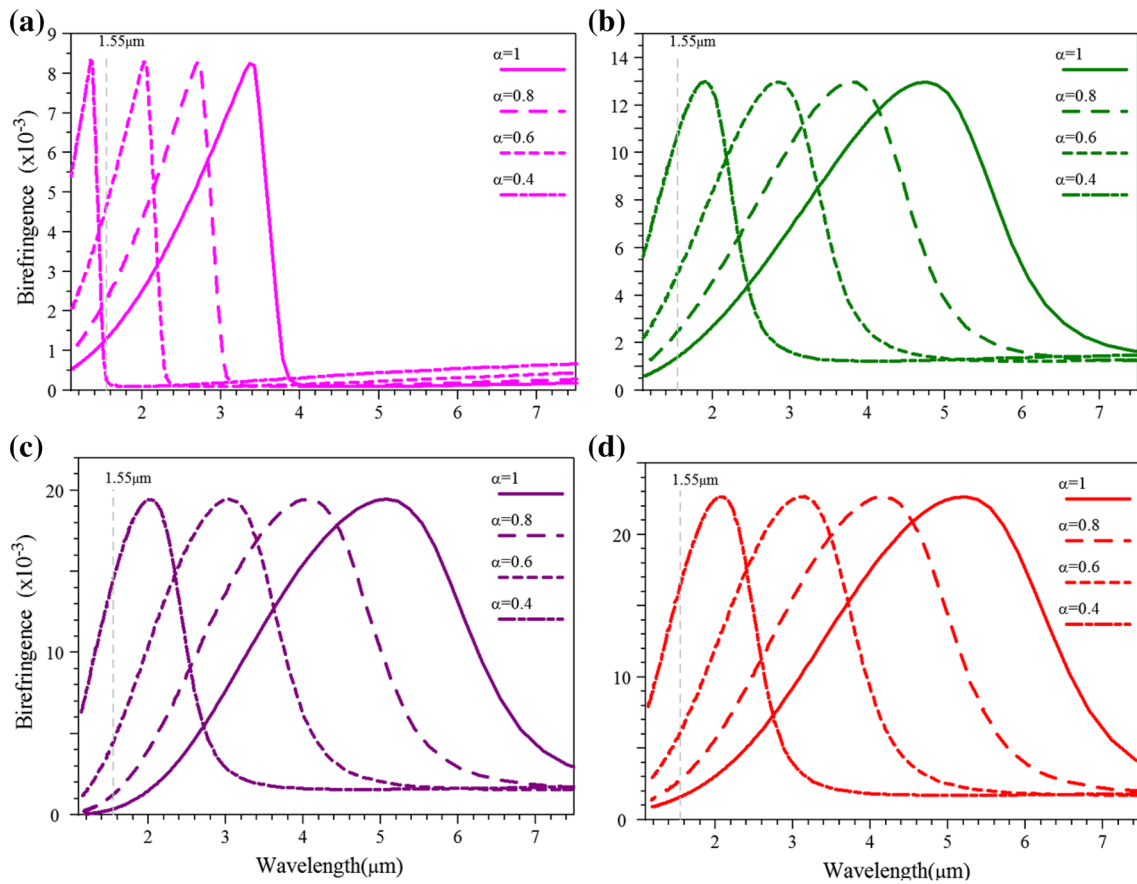


Fig. 5 Dependence of birefringence on wavelength for the HB-PCFs **a** Type 1, **b** Type 2, **c** Type 3, and **d** Type4, with various shrink ratios

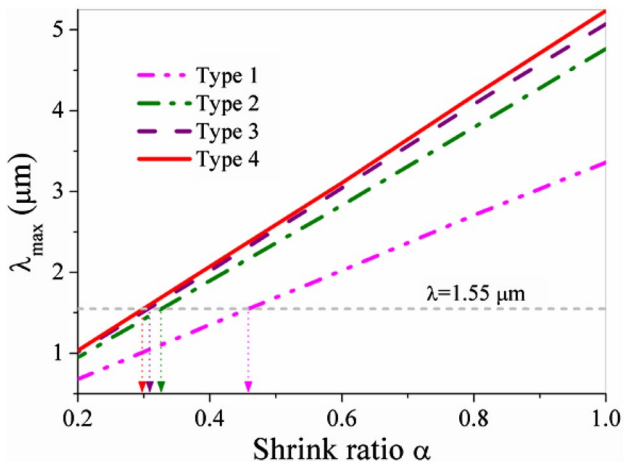


Fig. 6 Relationship between the λ_{\max} and the shrink ratio α for the HB-PCF Type 1 to Type 4

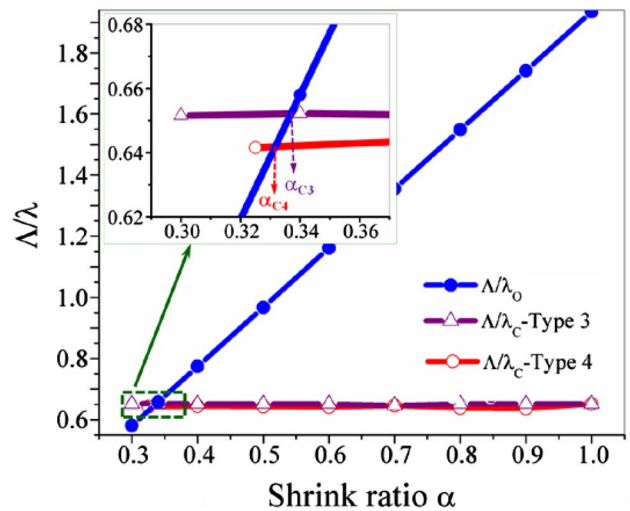


Fig. 7 Relationship between the Λ/λ_c for Type 3 and 4, the Λ/λ_o ($\lambda_o = 1.55 \mu\text{m}$) and the shrink ratio (α). The critical shrink ratios $\alpha_{c3}=0.3370$, $\alpha_{c4}=0.3316$ for HB-PCF Type 3 and 4, respectively

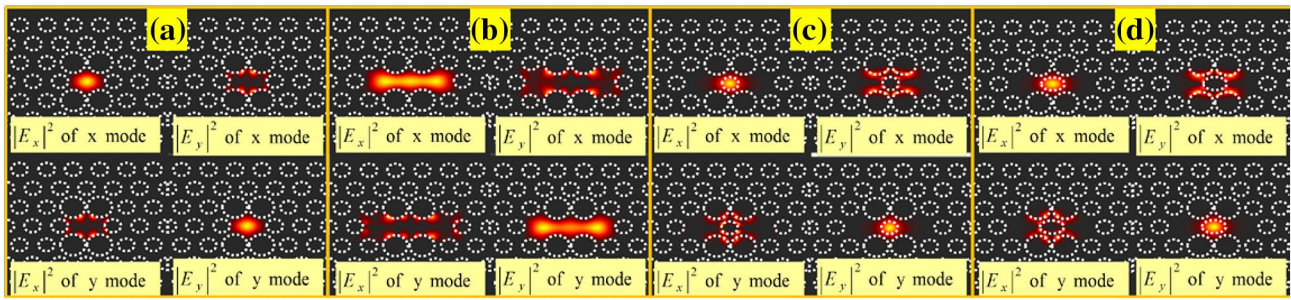


Fig. 8 Field patterns of the intensity components for the x - and y -polarized fundamental modes for the HB-PCF **a** Type 1, **b** Type 2, **c** Type 3, and **d** Type 4 at a wavelength of $1.55 \mu\text{m}$

$\lambda = 1.55 \mu\text{m}$, respectively. It is obvious in the figures that the degenerate doublet components of the fundamental mode in the HB-PCFs split significantly.

3.4 Confinement loss (L_C)

Up to now, the work has treated the maximum values of birefringence at a wavelength of $1.55 \mu\text{m}$. On the face of it, the maximum birefringence of $B = 22.65 \times 10^{-3}$ can be achieved using the design of Type 4 with a shrink ratio of $\alpha = 0.2992$. However, the fundamental mode should appear to dissipate seriously for an excessively compact structure, that is to say, a too small α . This behavior is caused by the effect of the modal filter or “modal sieve” of the cladding [23]. For shrinking the whole structure, the mode fields are shrunk to small ones simultaneously. The confinement losses will substantially increase while the fundamental mode field is small enough to pass through the modal sieve.

For the HB-PCF Type 3 and 4, to design a compromising structure by trading some birefringence for an acceptable loss, the dependences of the birefringence B and the confinement losses L_C on the shrink ratio α at a wavelength of $1.55 \mu\text{m}$ are displayed in Fig. 9a, b, respectively. As is obvious from the figures, if a small α is set to achieve a maximum birefringence at a wavelength of $1.55 \mu\text{m}$, the HB-PCFs are unrealistic owing to an extremely large loss. To choose an appropriate α for larger B and acceptable L_C , a reference loss of 0.5 dB/km is labeled in the figures. For the HB-PCF Type 3 in Fig. 9a, $L_C = 0.54 \text{ dB/km}$ is obtained if the $\alpha = 0.340$. However, the design will cause a multi-mode operation in the fiber due to $\alpha > \alpha_{c3}$. Therefore, a smaller α of 0.337 is selected, thus $B = 18.52 \times 10^{-3}$ and $L_C = 0.75 \text{ dB/km}$ is obtained for the HB-PCF Type 3. On the other hand, for the HB-PCF Type 4 in Fig. 9b, $B = 21.85 \times 10^{-3}$ and $L_C = 0.47 \text{ dB/km}$ is achieved if the α of 0.325 is chosen. Fortunately, the design for the HB-PCF Type 4 with large B and small L_C will enable the fiber to operate in single mode because it fit in with the condition

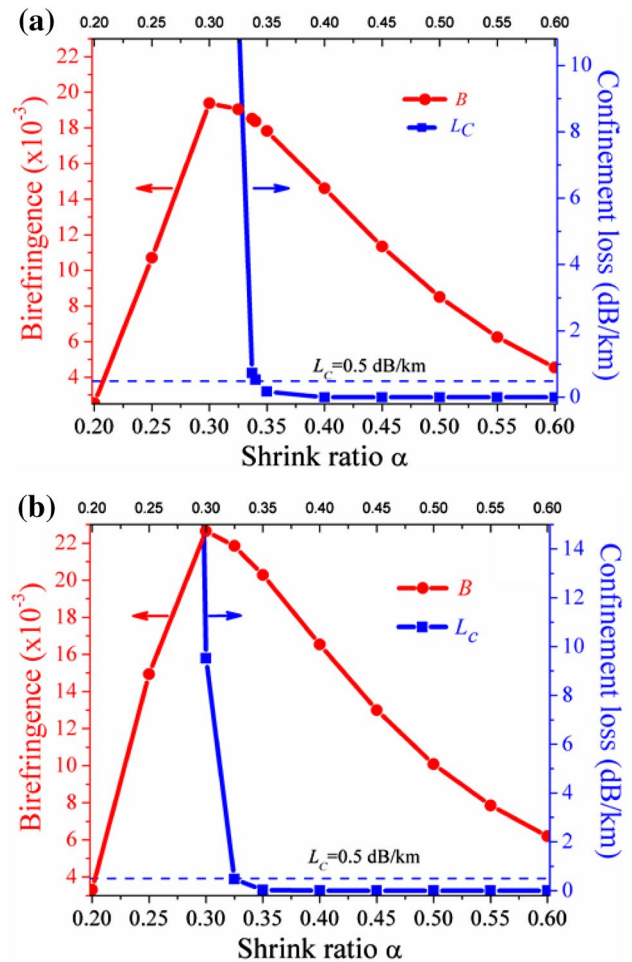


Fig. 9 Dependence of the birefringence B and the confinement loss L_C on the shrink ratio α at a wavelength of $1.55 \mu\text{m}$ for the HB-PCF **a** Type 3, and **b** Type 4

of $\alpha < \alpha_{c4}$. For clarity, Table 1 exhibits the designed geometric and optical parameters at a wavelength of $1.55 \mu\text{m}$ for the two designs. As per Fig. 9 and Table 1, the optical performances of the HB-PCF Type 4 are the better;

Table 1 Geometric and optical parameters at a wavelength of 1.55 μm for the designed HB-PCF Type 3 and 4

HB-PCF types	Shrink ratio α	$A(\mu\text{m})$	$d_1(\mu\text{m})$	$d_c(\mu\text{m})$	$d_x(\mu\text{m})$	$d_y(\mu\text{m})$	n_{core}	$B(\times 10^{-3})$	$L_C(\text{dB/km})$
Type 3	0.337	1.0110	0.9436	0.6066	0.6066	0.6066	1.56	18.52	0.75
Type 4	0.325	0.9750	0.9100	0.5850	0.8190	0.5850	1.56	21.85	0.47

however, the fabrication of the HB-PCF Type 3 is easier than the Type 4 due to the simple circular core rod.

3.5 Single polarization ranges (SPRs)

The HB-PCF may show single polarization in a wavelength range, which is called single polarization range (SPR) in this paper. The phenomenon of SPR can be described as follows. Figure 10a demonstrates the relationship between the effective indices of n_{eff}^x , n_{eff}^y , and n_{FSM} for the HB-PCF Type 4 with a shrink ratio of 0.4. As per the figure, for $\lambda < 2.268 \mu\text{m}$, both the n_{eff}^x and n_{eff}^y are larger than the n_{FSM} , thus both the splitting degeneration fundamental modes are well confined in the core region. For $\lambda > 2.895 \mu\text{m}$, both the n_{eff}^x and n_{eff}^y are smaller than the n_{FSM} , the modes should evanesce into the cladding. Within the wavelength range of $2.268 \mu\text{m} < \lambda < 2.895 \mu\text{m}$, which is a so-called SPR with a range of about 627 nm, the y-polarization mode should be cutoff due to $n_{\text{eff}}^y < n_{\text{FSM}}$, while the x-polarization mode still propagates due to $n_{\text{eff}}^x > n_{\text{FSM}}$. One of the splitting degeneration fundamental modes (y-polarization mode) is then filtered out in the wavelength range. Therefore, in the SPR, the fundamental mode is always linear polarization. Figure 10b exhibits the SPRs of all types of HB-PCFs in this work with shrink ratios of 0.3 to 0.8. Figure 10c shows the relationship between the birefringence, SPR, and wavelength for the HB-PCF Type 4 with the α of 0.325 (the proposed structure), 0.500, and 0.700, respectively. The hatch areas under the B curves represent the SPRs for each structure with various α .

4 Fabrication considerations

Several fabrication methods of PCF have been developed, such as stack-and-draw [24–26], extrusion [27], sol-gel casting [28], injection molding [29], drilling [30], and tapering [31]. The most common method is stack-and-draw technique, which is relatively fast, clean, low cost, and flexible. Similar to the fabrication process of general PCF, the proposed HB-PCFs can be easily fabricated using the stack-and-draw method. The PCF preform is realized by stacking a number of capillary silica tubes and rods with the same outer diameter, while the different inner diameters of d_1 and d_c (for tubes) will form the desired air-silica structure. The central rod is Ge doped in the center of silica rod, which is

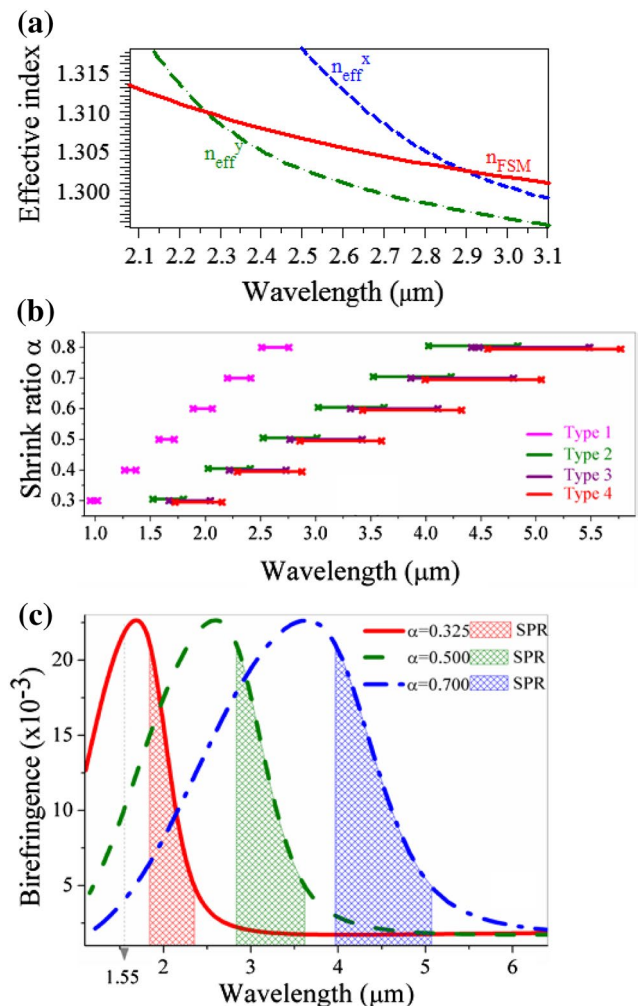


Fig. 10 **a** Relationship between the effective indices of n_{eff}^x , n_{eff}^y , and n_{FSM} for the HB-PCF Type 4 with a shrink ratio of 0.4. **b** The SPRs for all types of HB-PCFs with the shrink ratios of 0.3 to 0.8. **c** Relationship between the birefringence, SPRs, and wavelength for the HB-PCF Type 4 with the shrink ratios of 0.325, 0.500, and 0.700

just like a traditional MCVD fiber (Type 3) or an elliptical core fiber (Type 4). The refractive index of the central circular or elliptical rod is decided by the doping concentration of germanium. After the stacking process, the capillaries and rods are held together, and a HB-PCF, as shown in Fig. 2b–e, is then accomplished through the intermediate drawing and final drawing process [25, 26].

5 Conclusions

This study systematically designed and theoretically investigated an HB-PCF by adding some BEFs step by step in sequence. The modal birefringence increased even more whenever a BEF was introduced. By adding all the four BEFs, the modal birefringence of the HB-PCF was up to 22.65×10^{-3} at a wavelength of $5.24 \mu\text{m}$. To blue-tune the maximum birefringence wavelength toward the habitual wavelength of optical-fiber communications ($1.55 \mu\text{m}$), all the geometric parameters were shrunk with a shrink ratio α . Finally, the proposed HB-PCF with a high-index Ge-doped elliptic rod in the central core was designed. By trading some birefringence for an acceptable loss, the numeric results indicated that the modal birefringence and the confinement loss of the proposed HB-PCF Type 4 with geometric and optical parameters as shown in Table 1, are 21.85×10^{-3} and 0.47 dB/km , respectively, at the habitual wavelength $\lambda = 1.55 \mu\text{m}$ of the optical-fiber communications. Furthermore, the modal properties were examined and verified that the proposed HB-PCF should be operated in single mode.

There are quite a few published works which focus on the HB-PCF [1–14]; the basic principle of the works was breaking the array symmetry to enlarge the modal birefringence as well. In addition to systematically designing the HB-PCF by superimposing BEFs step by step to show the splitting of the degeneration doublet pair progressively, this work even more demonstrates an approach of blue-tune by shrinking or red-tune by expanding, examines the modal property to verify that the HB-PCF is operated in single mode, estimates the confinement loss and exhibits the approach of trading some birefringence value for an acceptable loss to design a compromising structure, and finally shows the SPRs of the fiber.

Acknowledgements The author is thankful for the financial support from the Ministry of Science and Technology, Taiwan, ROC, under Grant No. of MOST 105-2221-E-239-014.

References

1. K. Suzuki, H. Kubota, S. Kawanishi, M. Tanaka, M. Fujita, *Opt. Express* **9**, 676 (2001)
2. J. M. Hsu, G.S. Ye, D.L. Ye, *Fiber Integr. Opt.* **31**, 11 (2012)
3. J. M. Hsu, C.L. Lee, J.S. Horng, J.J.H. Kung, *Opt. Commun.* **298**, 125–128 (2013)
4. T.P. Hansen, J. Broeng, S.E.B. Libori, E. Knudsen, A. Bjarklev, J.R. Jensen, H.R. Simonsen, *IEEE Photon. Technol. Lett.* **13**, 588 (2001)
5. T. Nasilowski, et al, *Appl. Phys. B* **81**, 325 (2005)
6. M. Chen, S.G. Yang, F.F. Yin, H.W. Chen, S.Z. Xie, *Optoelectron. Lett.* **4**, 19 (2008)
7. A. Ortigosa-Blanch, J.C. Knight, W.J. Wadsworth, J. Arriaga, B.J. Mangan, T.A. Birks, P. St. J. Russell, *Opt. Lett.* **25**, 1325 (2000)
8. T.J. Yang, L.F. Shen, Y.F. Chau, M.J. Sung, D. Chen, D.P. Tsai, *Opt. Commun.* **281**, 4334 (2008)
9. Y.S. Sun, Y.F. Chau, H.H. Yeh, L.F. Shen, T.J. Yang, D.P. Tsai, *Appl. Opt.* **46**, 5276 (2007)
10. Y.S. Sun, Y.F. Chau, H.H. Yeh, D.P. Tsai, *Jpn. J. Appl. Phys.* **47**, 3755 (2008)
11. Y.S. Sun, Y.F. Chou Chau, W. Yang, H.H. Yeh, S.F. Wang, Y. Chu, Ci-Yao Jheng, J.M. Sung, *Jpn. J. Appl. Phys.* **52**, 062502 (2013)
12. K.Y. Yang, Y.F. Chau, Y.W. Huang, H.Y. Yeh, D.P. Tsai, *J. Appl. Phys.* **109**, 093103 (2011)
13. Y.F. Chou Chau, C.M. Lim, V.N. Yoong, M. N. S. Idris, *J. Appl. Phys.* **118**, 243102 (2015)
14. Y.F. Chau, *J. Modern Opt.* **58**, 1673 (2011)
15. Andrew A. B. Tio, P. Shum, Y.D. Gong, *Opt. Express* **11**, 2991 (2003)
16. L. Zhang, C. Yang, *Opt. Express* **11**, 1015 (2003)
17. X. Dong, H.Y. Tam, P. Shum, *Appl. Phys. Lett.* **90**, 151113 (2007)
18. R.A. Bergh, H.C. Lefevre, H.J. Shaw, *J. Lightwave Technol.* **LT-2**, 91 (1984)
19. K. Saitoh, M. Koshiba, *J. Lightwave Technol.* **24**, 4729 (2006)
20. H. Malitson, *J. Opt. Soc. Am.* **55**, 1205 (1965)
21. T.A. Birks, J.C. Knight, P. St. J. Russell, *Opt. Lett.* **22**, 961 (1997)
22. J. Broeng, D. Mogilevstev, S.E. Barkou, A. Bjarklev, *Opt. Fiber Technol.* **5**, 305 (1999)
23. P. St. J. Russell, *J. Lightwave Technol.* **24**, 4729 (2006)
24. J. C. Knight, T. A. Birks, P. St. J. Russell, D.M. Atkin, *Opt. Lett.* **21**, 1547 (1996)
25. J. M. Hsu, C. W. Yao, J. Z. Chen, *J. Lightwave Technol.* **33**, 2240 (2015)
26. M. Delgado-Pinar, J. Cascante-Vindas, et al., *IEEE/ICTON*, **2007**, 157 (2007)
27. V.V.R.K. Kumar, A.K. George et al., *Opt. Express* **10**, 1520 (2002)
28. H. E. Hamzaoui, L. Bigot, et al., *Opt. Mater. Express* **1**, 234 (2011)
29. Q. Coulombier, L. Brilland, et al., *Proc. SPIE* **7598**, 75980O (2010)
30. N.A. Issa, M.A.V. Eijkelenborg, M. Fellew et al., *Opt. Lett.* **29**, 1336 (2004)
31. P. Domachuk, A. Chapman, E. Mägi, M.J. Steel, H.C. Nguyen, B.J. Eggleton, *Appl. Opt.* **44**, 3885 (2005)